Ce- and Ni-codoped Double PrBaMn$_2$O$_5$ Perovskite

as a Ceramic SOFC Anode

Praveen B. Managutti,[a] Yeting Wen,[b] T.C. Hansen,[c] Vincent Dorcet,[d] Serge Paofai,[d] Pascal Briois,[e] Kevin Huang,[b] * and Mona Bahout [d*]

[a] Chemical Crystallography Laboratory, Khalifa University of Science and Technology, Abu Dhabi, P.O. Box 127788, United Arab Emirates

[b] Department of Mechanical Engineering, University of South Carolina, Columbia, SC, 29208, USA

[c] Institut Laue-Langevin, 71 avenue des Martyrs CS 20156, 38042 Grenoble Cedex 9, France

[d] Univ Rennes, CNRS, ISCR (Institut des Sciences Chimiques de Rennes) - UMR 6226, F-35000 Rennes, France

[e] FEMTO-ST Institute (UMR CNRS 6174), Université Bourgogne Franche-Comté, UTBM, F-25200 Montbéliard Cedex, France

Abstract

This study explores the efficacy of cerium introduction, both singly and in combination with nickel, into PrBaMn$_2$O$_{5+\delta}$ (PBM) structures to enhance solid oxide fuel cells (SOFC) anodes. We synthesized Pr$_{1-x}$Ce$_x$BaMn$_2$O$_{5+\delta}$ compositions for x values of 0.05 (PrCe5) and 0.1 (PrCe10), as well as a nickel-doped variant (PrCe5Ni), assessing their performance under H$_2$-3% H$_2$O reducing conditions pertinent to SOFC anode operations. Our findings reveal that the PrCe5 composition exhibits a thermal expansion coefficient (TEC) that not only improves upon the Ce-free counterpart but also aligns closely with the TEC standards of prevalent SOFC electrolytes. A notable advance was achieved with the application of a 3.5 µm GDC buffer layer through physical vapor deposition, effectively mitigating chemical interactions between PBM-based anodes and YSZ electrolytes, a concern highlighted by *in situ* neutron diffraction analyses. Electrochemical impedance spectroscopy, conducted over 220 hours in an H$_2$-3% H$_2$O atmosphere at 750 °C, demonstrated that the optimal 3.5 µm thickness of the GDC buffer

layer significantly minimizes the area-specific resistance (ASR) degradation rate to 0.002 Ω cm^2/h, markedly outperforming both thinner (1 µm) and thicker (8 µm) GDC layers which showed higher degradation rates of 0.15-0.2 Ω cm^2/h. Moreover, cerium doping fosters superior microstructural stability and obviates barium diffusion, thereby suggesting an enhanced durability of the doped anodes over their lifespan. Integrating nickel into the PrCe5 structure halved the ASR to 0.5 Ω cm^2 at 750 °C, situating it well within the ideal performance range for SOFC anodes. The enhancement brought about by simultaneously doping PBM with cerium and nickel, which fundamentally relies on the critical contributions of defect chemistry and crystal structure, highlights the significance of these fields in creating sophisticated materials for energy-related applications.

1. Introduction

Solid Oxide Fuel Cells (SOFCs) represent a cutting-edge technology with great potential for the efficient and eco-friendly generation of power from hydrogen.[1-7] However, current SOFCs suffer from various obstacles limiting their market entry. Challenges related to the anode are prominent among these issues: severe reducing environment and high temperature. During operation, it must remain thermally stable and maintain redox stability to avoid cracking and mechanical compatibility with the electrolyte to prevent delamination. Conventional nickel–yttria stabilized zirconia (Ni–YSZ) cermet anodes face issues in terms of Ni agglomeration, redox instability due to Ni reoxidation,[8] and long-term deactivation caused by sulfur poisoning and coking when used with hydrocarbon fuels.[9-11] Mixed Ionic and Electron Conducting

(MIEC) perovskite oxides have been considered as alternatives for Ni-based cermets to mitigate the aforementioned problems,[6] but their electrochemical activity is insufficient. It is well known that cerium, owing to its variable oxidation states (Ce^{3+} and Ce^{4+}), can contribute to oxygen ion conductivity and electrocatalytic activity, important for the anodic and cathodic reactions in SOFCs.[12] For instance, substitution of 10 at. % of cerium at the A-site of $La_{0.75}Sr_{0.25}Cr_{0.5}Mn_{0.5}O_3$ has been shown to enhance SOFC's anodic performances under H_2 and CH_4.[13] Likewise, the Ce-doped anode materials $Ce_xLa_{0.75-x}Sr_{0.25}Cr_{0.5}Mn_{0.5}O_3$,[13] $Ce_xSr_{1-x}Cr_{0.5}Mn_{0.5}O_3$,[14] $(Pr,Ce)MnO_3$,[15] $La_{0.3}Ce_{0.1}Sr_{0.5}Ba_{0.1}TiO_{3-\delta}$,[16] and $La_{0.23}Ce_{0.1}Sr_{0.67}TiO_{3-\delta}$[17] have also been reported with enhanced electrooxidation kinetics in comparison with Ce-free compositions. Finally, infiltration of samarium-doped ceria (SDC) in combination with NiO into $La_{0.6}Sr_{1.4}MnO_{4+\delta}$ significantly enhanced the electrochemical activity for H_2 and CH_4 fuels oxidation.[18] These observations underscore the significance of cerium in catalysis and electrocatalysis.

The double-layered perovskite manganites, such as $PrBaMn_2O_{5+\delta}$ (PBM), have recently attracted attention as potential anode materials for their robust thermal stability in reducing atmospheres. However, enhancing their electrocatalytic performance remains a challenge.[19,20] Although various transition metals, metal alloys, and metal oxides have been incorporated into PBM to boost its electrochemical capabilities,[19-22] the potential benefits of cerium inclusion have not yet been explored. This presents an untapped opportunity to further elevate the functionality of PBM-based anode materials.

This study seeks to examine the impact of cerium substitution, either alone or in conjunction with nickel, on PBM anode performance for hydrogen oxidation. Nickel-doping at the B-site of the layered perovskites enhances electrochemical performance by promoting metal exsolution, as reported for PBM.[20, 21] The combined effects of cerium mixed valence states and nickel metal exsolution when doping with Ce and Ni influence both ionic and electronic

conductivity. These changes are driven by oxygen vacancy formation, lattice distortion, valence state alterations, band structure modifications, and defect-induced conductivity. The chemical reactivity between a Ce-doped PBM anode and 8YSZ electrolyte was monitored through *in situ* neutron diffraction in air up to 950 °C. To prevent chemical reactivity between the electrode and electrolyte,[23] a dense gadolinia-doped ceria (GDC) buffer layer was deposited on commercial 8YSZ disks *via* physical vapor deposition (PVD), a process that does not involve high-temperature sintering. The impact of GDC thickness on the electrochemical performance and stability in a hydrogen atmosphere (with 3% H_2O) was investigated by electrochemical impedance spectroscopy.

2. Experimental

2.1 *Synthesis and characterization*

Polycrystalline $Pr_{1-x}Ce_xBaMn_2O_{5+\delta}$ with x = 0, 5, 10, 15 % (henceforth referred to as PBM, PrCe5, PrCe10, PrCe15, respectively) and $Pr_{0.95}Ce_{0.05}BaMn_{1.9}Ni_{0.1}O_{5+\delta}$ (henceforth referred to as PrCe5Ni) were prepared by the citric acid sol gel method. Stoichiometric amounts of $Pr(NO_3)_2 \cdot 6H_2O$ (Aldrich, 99.9%), $Ce(NO_3)_2 \cdot 6H_2O$ (Aldrich, 98%), $Ba(NO_3)_2$ (Aldrich, 99%), $Mn(NO_3)_2 \cdot 4H_2O$ (Aldrich, 98%), $Ni(NO_3)_2 \cdot 6H_2O$ (Aldrich, 98.5 %) were dissolved in distilled water. Ethylene glycol (EG) and citric acid (CA) were added in the molar ratio to the total metal ions (M) CA:EG:M of 1.5: 3:1. The pH value was fixed to ~ 8 by adding ammonium hydroxide to enhance cation binding to the citrate and avoid the precipitation of individual hydroxides.[24] The solution was stirred on the hot plate until a resin formed which was subsequently calcined at T ~ 550 °C overnight. The solid precursors were ground, pressed in pellets (13 mm diameter, 2-3 mm thickness) and sintered under 1% H_2/N_2 at 1000 °C for 48 h except PrCe5Ni which was sintered in air at 950 °C for 24 h to incorporate nickel ions into the oxide lattice. The as-prepared sample was heated in 5% H_2/Ar at 875 °C for 42 h to exsolve the Ni particles on the oxide

surface resulting in the reduced sample denoted as PrCe5Ni-H. To assess redox stability, the hydrogen-annealed samples were heated in air at 800°C, resulting in the formation of the oxidized samples labeled as PrCe5-A, PrCe10-A, and PrCe5Ni-A.

All the samples were characterized by powder X-ray diffraction (XRD) using a D8-A25-Advance (Bruker) diffractometer operating in Bragg-Brentano geometry with a Cu-K$_{\alpha 1}$ radiation equipped with a silicon strip Lynxeye detector. Structural information was obtained by Rietveld refinements using the FullProf Suite program and its graphical interface WinPLOTR.[25] The surface microstructure was examined by scanning electron microscopy (SEM) using a JEOL JSM 7100 F EDS EBSD Oxford. Transmission electron microscopy (TEM) was done using a JEOL JEM-2100 LaB$_6$ instrument operated at 200 kV equipped with energy-dispersive spectroscopy (EDS) (OXFORD). A small amount of powder was added to ethanol, followed by ultrasonic mixing to achieve a particle dispersion. A few drops of the suspension were deposited on carbon-coated grids. Micrographs were digitally acquired on a 2 × 2 k charge-coupled device camera using a Gatan Imaging Filter system.

2.2 *Chemical reactivity with the YSZ electrolyte monitored by neutron diffraction.*

Redox stability and chemical reactivity were monitored by Neutron Powder Diffraction (NPD) on the high-flux two-axis D20 diffractometer at the *Institut Laue-Langevin* (ILL, Grenoble, France)[26]. The configuration replicates that outlined previously.[20, 27-29] We selected a take-off angle of 90 degrees from the (115) plane of a germanium monochromator, which yielded $\lambda \sim 1.54$ Å and a resolution of $\Delta d/d \sim 2.9 \times 10^{-3}$. This setup maintains a high flux, $\sim 1.6 \times 10^7$ neutrons per square centimeter per second. The sample consists of a 2-gram pellet mixture of PrCe5:8YSZ in a 50:50 wt. % ratio, which is loaded into an 8 mm quartz cell. A heating and cooling cycle was performed under synthetic air, spanning a temperature range from 20 to 950 °C at a rate of 10 °C/min. Data were collected at five-minute intervals throughout this thermal

cycle. Additionally, isothermal data sets were recorded over a period of 2 h both at the start and end of the cycle, as well as at the peak temperature of 950 °C. The Rietveld refinement was performed using the FullProf Suite software. Background modeling was achieved through a linear interpolation function, and the profile was fitted using the Thompson-Cox-Hastings Pseudo-Voigt function.[30] The standard deviation values were corrected according to Berar's and Lelann's. description.[31]

2.3 *Symmetrical cell fabrication*

Symmetrical cells were fabricated using commercial 230 µm-thick 8YSZ disks, each measuring 25 mm in diameter (Tosoh). To prevent ionic interdiffusion and chemical reactions, a $Ce_{0.9}Gd_{0.1}O_{1.95}$ (GDC) buffer layer was deposited on both sides of the electrolyte through physical vapor deposition.[29, 32] The experimental setup comprises a 100-litre Alcatel SCM 650 sputtering chamber, evacuated by an integrated system that includes an XDS35i Dry Pump and a 5401CP turbo-molecular pump. This chamber is outfitted with a trio of magnetron targets, each 200 mm in diameter, and a rotating substrate holder of 620 mm diameter, positioned parallel to the targets at an approximate distance of 110 mm. The separation between the central axis of the targets and that of the substrate holder is 170 mm. For sputter deposition, we employ a 10 at. % Gd-Ce target, powered by an Advanced Energy dual generator capable of pulsating DC. This generator facilitates control over the discharge's current, power, and voltage. The deposition process is regulated by a Plasma Emission Monitoring system, which operates on a closed-loop control mechanism and utilizes optical emission spectroscopy to monitor plasma emissions. For this study, we have set the discharge current at a steady 2.5 A, while maintaining the total pressure at approximately 0.2 Pa. Additional methodological details have been documented elsewhere.[33] Various thicknesses of the GDC layer, ranging from 1 to 13 µm, were investigated. The anode slurry, consisting of 50 wt. % electrode powder and 50 wt. % organic

binder (V-006, Heraeus), was screen-printed on both sides of the GDC/8YSZ/GDC electrolyte and calcined in air for 2 hours at $T = 1100$ °C, a condition under which no reaction occurred with GDC. However, increasing the temperature to 1200 °C could potentially trigger a reaction between YSZ and GDC, potentially leading to the formation of $(Zr,Ce)O_2$ solid solutions,[23, 34] which display reduced ionic conductivity. The electrode had an effective area of 1.3 cm² and an approximate thickness of 20 μm. Gold paste (C5756, Heraeus) was applied atop each electrode to improve the contact between the electrode and the current collectors by filling in any microscale gaps or irregularities on the surface, which might otherwise increase contact resistance. Silver mesh and silver wire served as the current collectors. Subsequently, the components were heated in air at 700 ºC for 2h to ensure proper attaching.

Prior to and following the EIS tests, the interfaces between the electrode, GDC, and YSZ were examined using a Scanning Transmission Electron Microscope (STEM, Hitachi HD-2000) and energy dispersive X-ray spectroscopy (EDS SDD, X-Max 80 mm^2 Oxford Instruments AZtecEnergy, England) to evaluate the microstructural integrity and detect any changes at the nanoscale level. Occasionally, the surface of the electrodes underwent XRD analysis (Rigaku MiniFlex II device, utilizing Cu Kα radiation) before and after conducting the electrochemical tests. This analysis is aimed to identify any crystalline phase changes or reactions that may have occurred during electrode processing or testing. The XRD patterns were acquired over a 2θ range of 10- 80°, with a step size of 0.02 ° and a scanning rate of 2 ° min^{-1}.

2.4 *Electrochemical Measurements*

The EIS spectra were recorded using a Solartron 1470/1455B multi-channel electrochemical station, with frequency range of 10^5 Hz-10 mHz and an AC signal amplitude of 10 mV under open-circuit voltage (OCV) conditions. These spectra were analyzed using the Zview software.

All impedance data were normalized to the electrode area (1.3 cm^2) and were fitted using an equivalent circuit that included inductance to account for the electrical lead effects and a series resistance (R_s), primarily attributed to the electrolyte conductivity. For better comparison of the electrode polarization resistances, all EIS data were plotted in the quadrant of positive -Z'/Z' values. The measurements were conducted in temperature range of 750-450 °C in a wet H$_2$-3% H$_2$O environment, with a flow rate of 100 mL min^1. The measurements started once the system achieved stability at 750 °C.

3. Results and discussion

3.1 *Structural analysis*

Figure 1 shows X-ray diffraction patterns from as-prepared PBM, PrCe5, PrCe10, and PrCe15. The main diffraction peaks corresponded closely with the predicted patterns for PrBaMn$_2$O$_6$ (JCPDS # 01-076-6163). In PrCe15, the presence of a peak at approximately $2\theta = 28°$, which can be attributed to the (111) plane of CeO$_2$ (JCPDS # 34.0394) indicates that the solubility limit has likely been surpassed by the 15 mol % concentration of Ce. The increase in lattice parameters, as evidenced by Figure S1 & Table S1, suggests that Ce^{3+} ions have substituted Pr^{3+} ions. This assertion is corroborated by the ionic radii of the involved ions: Ce^{3+} has a larger ionic radius (~1.143 Å) in an eight-fold coordination than Pr^{3+} (1.126 Å), whereas the ionic radius of Ce^{4+} is smaller (0.97 Å).[35]
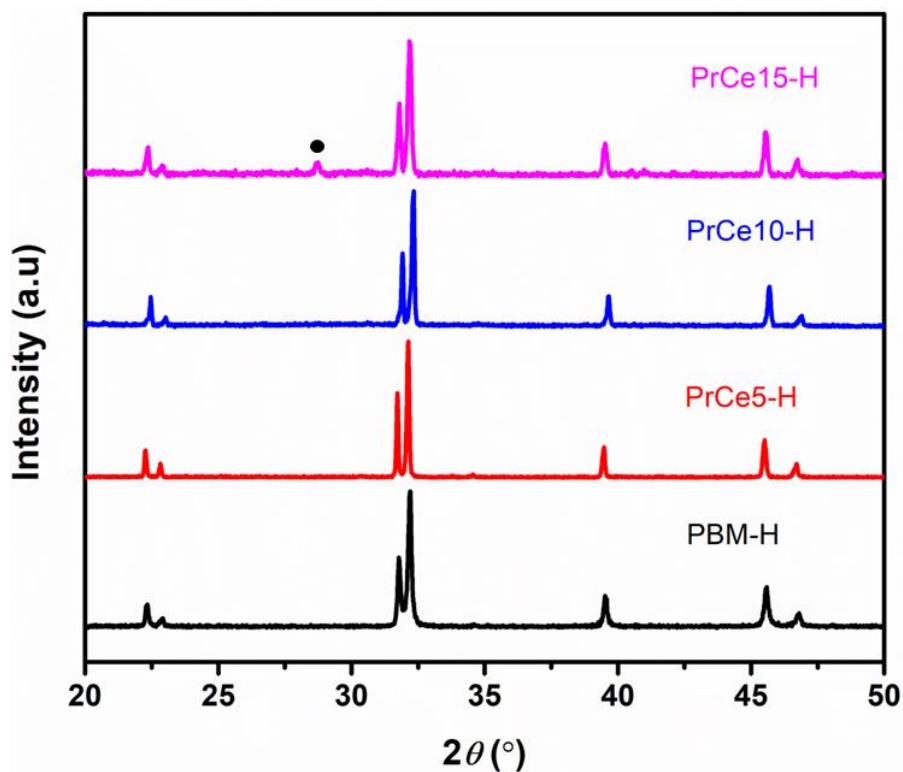
Figure 1. XRD patterns of as-prepared layered double perovskites. The peak from CeO$_2$ (●) in PrCe15-H is highlighted.

From the multiphase Rietveld analysis, the CeO$_2$ phase in PrCe15 was estimated at 2.4 (2) wt.%, signifying a solubility limit of 8.6 cerium at. %. Given that concentration falls short of the intended 10 at. % in the PrCe10 composition, our investigation will be more effectively concentrated on the PrCe5 and PrCe5Ni compositions, compared with the Ce-free PBM one.

The thermal stability of PBM and PrCe5 was studied in air at 800 °C to check if they can withstand typical SOFC operation environments. As shown in Figure S2, the XRDs of the oxidized samples, referred to as PrCe5-A and PBM-A, are inherent to single-phase materials that share the same *P*4/*mmm* structure of the as-prepared compositions validating their potential for long-term use in SOFC applications. Both a and c lattice parameters have decreased (Table S2) due to the change in manganese oxidation state from Mn$^{+2.5}$ to Mn$^{+3.5}$ as a consequence of oxygen ion incorporation into the (Pr/Ce)O layer.[36, 37] Indeed, the substantial capability for oxygen intercalation and release in layered perovskites has been confirmed through thermogravimetric analysis,[38, 39] neutron diffraction studies,[40] and coulometric titration,[41] with

$PrBaMn_2O_{5+\delta}$ particularly exhibiting a remarkable capacity for extensive variations in oxygen stoichiometry[42] highlighting its potential for applications in SOFCs.[43]

3.2 *PrCe5Ni sample*

To synthesize the $Pr_{0.9}Ce_{0.05}BaMn_{1.9}Ni_{0.1}O_{5+\delta}$ composition (referred to as PrCe5Ni) and to ensure the incorporation of nickel ions into the oxide lattice, the powder mixture was annealed in air at 950 °C for 12 hours. The XRD pattern presented in Figure S3 indicates the presence of both orthorhombic and hexagonal perovskite phases, which agrees with previous reports on related compositions.[20]

To exsolve the nickel particles, the PrCe5Ni sample underwent a heat treatment in a 5% H_2/N_2 atmosphere at $T \sim 850$ °C. This elevated temperature removed oxygen from the PrOx layer resulting in a structural reconstruction to a layered double perovskite ($a = 3.9748$ (1) Å, $c = 7.7651$ (2) Å) coupled with the complete exsolution of nickel (~1.3 wt.%), as confirmed by Rietveld analysis. The XRD pattern in Figure S4 revealed trace amounts of Pr_2O_3 and $PrMnO_3$, each less than 1 wt.%, were detected.

To evaluate the reversibility of nickel exsolution and dissolution, the PrCe5Ni sample was heated in air at a temperature of ~ 800 °C overnight. The XRD pattern in Figure S5 indicates that the Pr_2O_3 and $PrMnO_3$ impurity phases as well as most of the nickel dissolve into the layered perovskite structure. Nevertheless, small amounts of NiO (~ 0.30 wt.%, representing ~ 20 % of the Ni content) and CeO_2 (~ 0.22 wt.%) remained, which may further dissolve into the structure at higher temperatures. Given the difficulties associated with nickel insertion in layered double perovskites,[20] this significant reversibility could be advantageous for catalyst regeneration, potentially enhancing the anode longevity. Following oxidation, the cell experienced a contraction with parameters $a = 3.90150$ (5) Å and $c = 7.7490$ (1) Å, leading to a volume decrease of approximately 1.3%. While this volumetric change remains high, it is

markedly less than the ~ 40% expansion of nickel when it is oxidized within a Ni-YSZ cermet.[44] The addition of a ceramic phase, such as GDC, to the electrode material could lead to a more uniform distribution of mechanical stress, thus mitigating the effects of this expansion.

Analysis of the surface of the as-prepared sample by scanning electron microscopy (SEM) reveals particles with irregular, rounded, granular morphology, as shown in **Figure 2a**. These particles exhibit some aggregation and display variable size, but predominantly fall within the nanometer scale. The surface of the reduced sample in Figure 5b has a rough texture showing a multitude of spherical or near-spherical particles uniformly distributed. Additionally, the crystal reconstruction upon reduction seems to have increased the grain size of the support. Interestingly, on the surface of the reoxidized sample in Figure 5c, the exsolved particles are no longer observed, and the grain size of the support remained consistent following oxidation.
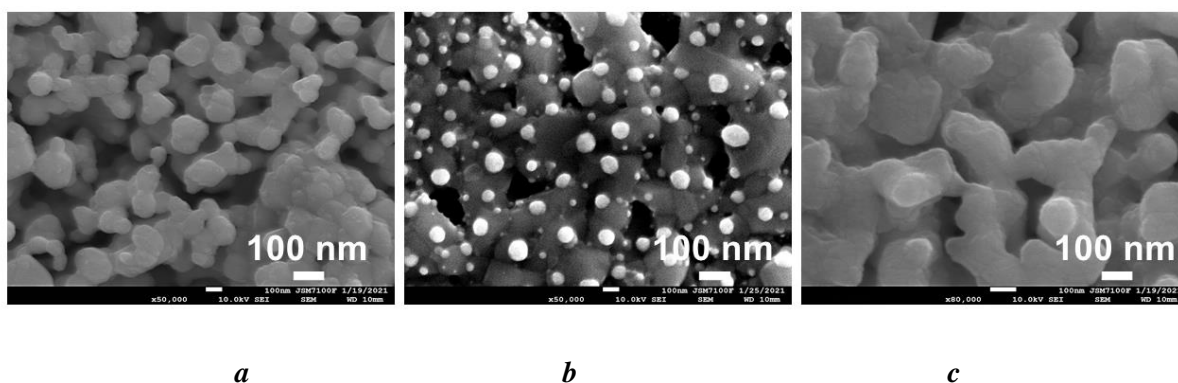

a   *b*   *c*

Figure 2. SEM images of (a) as prepared, (b) reduced where the exsolved Ni particles appear as white spheres, and (c) oxidized PrCe5Ni samples.

A further detailed investigation was carried out using Transmission Electron Microscopy (TEM). This advanced technique revealed that the exsolved particles in PrCe5Ni are ~ 40 nm in diameter, as depicted in Figure 3.
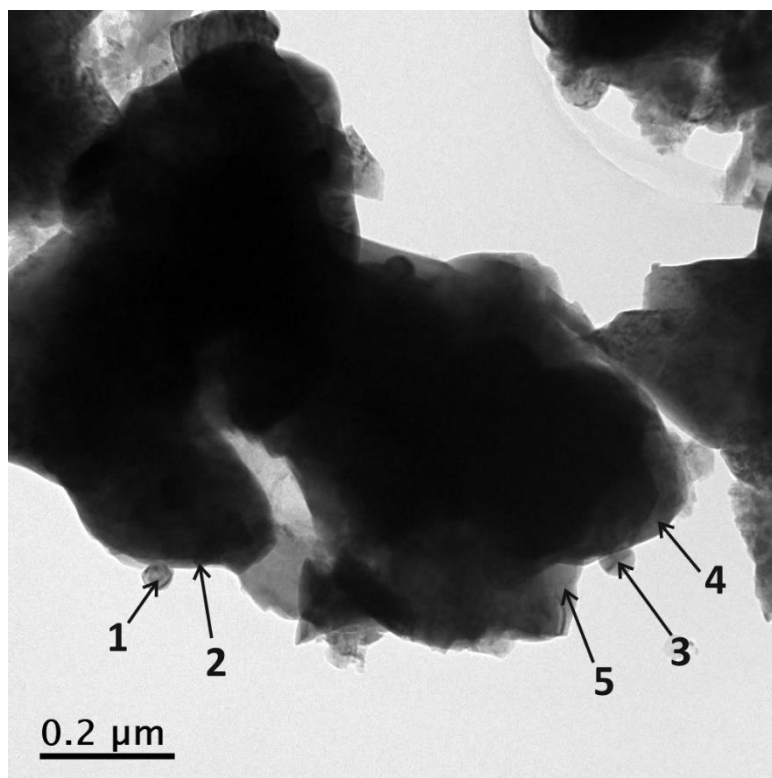
Figure 3. TEM bright field image of reduced PrCe5Ni, with corresponding EDS metal composition in at.%. Points labeled '1' and '3' indicate nickel particles, detailed in Table 1.

Table 1 presents the EDS quantification of five different points. Points 1 and 3 are dominated by Ni, and contain only trace amounts of Mn, Ba, Pr and Ce, suggesting that they are nickel particles. Points 2, 4, and 5 show a similar composition with a high presence of Mn, Ba, and Pr, and an exceptionally low presence of Ni and Ce suggesting that these points are in the perovskite phase. The slight composition variations between these points could be due to slight changes in composition or measurement inaccuracy. The significant difference in composition between points 1 and 3 *versus* points 2, 4, and 5 indicates that the sample is a composite material corresponding to Ni catalyst nanoparticles and a perovskite ceramic anode material. It should be emphasized that EDS offers a semi-quantitative evaluation, frequently supplemented by other methods for more accurate quantification. Typically, EDS can achieve an accuracy within a few percent for elements that are abundant in a sample. However, for elements present in smaller quantities, such as cerium with a nominal concentration of 1.25 at. % in the PrCe5Ni sample, the relative error could approach 10-20%. Therefore, the possibility that cerium

underwent an exsolution process as observed in Ni/Ce co-doped titanates resulting in nickel particles enveloped by a CeO$_2$ shell cannot be definitively ruled out.[45]

Table 1: Quantitative EDS Analysis for Locations 1 to 5 as presented in Figure 3.

	Mn	Ni	Ba	Ce	Pr
1	0,73	98,79	0,39	0,02	0,06
2	44,93	0,08	27,01	1,46	26,52
3	0,96	97,67	0,57	0,12	0,68
4	43,18	0,11	27,97	1,26	27,48
5	43,31	0,04	28,10	1,84	26,71

3.3 *Chemical Reactivity with the Electrolytes*

Understanding the chemical compatibility between potential electrode and electrolyte materials is crucial in crafting advanced ceramics with superior properties. To this end, the PrCe5/GDC powder mixture underwent a heat treatment at 1200 °C for 3h. Comparative analysis of diffraction patterns, presented in Figure S6, before and after this thermal exposure reveals exclusive peaks corresponding to PrCe5 and GDC. This observation strongly indicates favorable chemical compatibility between the materials, reinforcing their potential to synergize effectively in high-temperature ceramic applications. Conversely, after firing the PrCe5/YSZ mixture at 1200 °C for 3 hours, new diffraction peaks at $2\theta = 30°$ and $33°$ attributed to BaZrO$_3$ (JCPDS# 06-0399) were observed in the diffraction patterns as illustrated in Figure S7. The undesirable chemical interaction between PrCe5 and YSZ leads to the formation of additional phases that could undermine the material's performance and stability.

To have deeper insight into the reactivity of the PrCe5 electrode material with 8YSZ, neutron patterns were collected on a PrCe5/YSZ pellet on heating in air up to 950 °C. The structure of PrCe5 was refined in the S.G. *P4/mmm* consistent with the absence of Mn^{3+}/Mn^{2+} charge ordering[46] and the structure of 8YSZ was refined in the S.G. *Fm-3m*. The pattern obtained at T = 20 °C is displayed in Figure S8 and the structural parameters are listed in Table S3.

Upon heating, oxidation of PrCe5 proceeds in the temperature range $T \sim$ 260-315 °C as shown on Figure S9. A two-phase model related to the reduced and oxidized phases was needed to fit representative data displayed in Figure 10. This is indicative of a heterogeneous reaction front within the sample, with oxidation initiating at the grain boundaries and progressing inwards. As the temperature increases, the peak intensities for the reduced phase diminish, while those corresponding to the oxidized phase become more pronounced, suggesting the conversion of Mn ions from a lower to a higher oxidation state. The reversible oxygen intercalation in PBM suggests that this electrode can repeatedly absorb and release oxygen without significant degradation. This property is highly beneficial for SOFCs as it can potentially improve their efficiency and lifespan. In addition, reversible oxygen can directly affect the oxygen ion conductivity and the overall electrochemical performance particularly during cycling conditions where oxygen levels fluctuate.

Rietveld analyses of the PrCe5/8YSZ composite neutron pattern recorded at the highest temperature reached in the neutron experiment, T = 950 °C, Figure S11, and after the thermal cycle in air, Figure 4, reveal the dominant peaks of $BaZrO_3$. These observations not only confirm the chemical reactivity between PrCe5 and 8YSZ at elevated temperatures but also parallel the reactivity with YSZ of other barium-rich electrode compositions, such as $Ba_{0.5}Sr_{0.5}Co_{0.8}Fe_{0.2}O_{3-\delta}$ (BSCF), occurring at T = 900 °C,[47] and even reported at temperatures as low as 800 °C.[48]
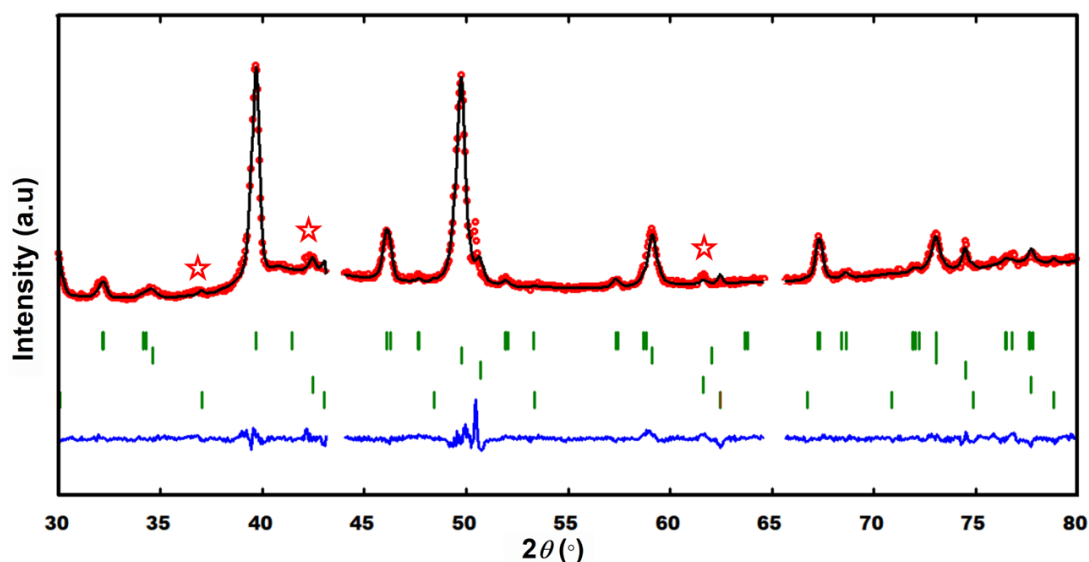
Figure 4. Neutron pattern for PrCe5/8YSZ collected at the end of the cycle in air using a wavelength of 1.54 Å. Few peaks from BaZrO₃ (4th row) are highlighted. The tick marks for PrCe5 (1st row), 8YSZ (2nd row), and the thermocouple material (3rd row) are delineated.

Figure S12 delineates the relationship between temperature and the refined lattice parameters for PrCe5 and 8YSZ upon cooling in air. With PrCe5 crystallizing in a tetragonal lattice, two distinct linear thermal expansion coefficients, namely α_a for the basal plane and α_c for the c-axis, were obtained. Assuming an even distribution of grain orientation post-electrode manufacturing, the calculated average linear thermal expansion coefficient (TEC) for 8YSZ is estimated at $\sim 10.7(1) \times 10^{-6}$ K^{-1} in consistency with published values of $10\text{-}11 \times 10^{-6}$ K^{-1}.[49-51] The TEC value for PrCe5 of $\sim 13.8(1) \times 10^{-6}$ K^{-1}, lower than the previously reported value of $16.8(2) \times 10^{-6}$ K^{-1} for the Ce-free composition,[43] places PrCe5 even more closely within the range of common electrolytes such as lanthanum gallate magnesium strontium oxide (LSGM) with TEC of $\sim 11\text{-}12 \times 10^{-6}$ K^{-1},[52] and GDC with TEC of $\sim 12\text{-}13 \times 10^{-6}$ K^{-1}.[53, 54]

4. Electrochemical performance

The EIS measurements aim to identify the apparent rate-limiting step(s) for hydrogen oxidation, to optimize the operating conditions.[6] The measurements were collected in wet hydrogen

atmosphere for electrolyte-supported symmetrical cells on a 250 µm-thick 8YSZ electrolyte. The 8YSZ discs were coated with a dense GDC layer to prevent reaction with Ba-based electrodes. The buffer layer thickness plays a crucial role in electrode performance. A thin GDC layer may fall short in preventing cation diffusion between the electrode and electrolyte, causing stability issues and degradation over time. Conversely, a thick layer provides a superior diffusion barrier, but might impede the flow of ions and electrons, thereby limiting the overall electrode performance. Therefore, we examined the effects of GDC thicknesses on electrode performance.

4.1 Impact of the GDC thickness on the electrochemical performance

Figure 5 shows Nyquist plots from electrochemical impedance spectroscopy at 750 °C under H_2-3% H_2O, for the PBM, PrCe5, and PrCe5Ni electrodes on different GDC buffer layer thicknesses of 1 µm, 3 µm, and 8 µm.

Focusing specifically on the 1 µm-GDC buffer layer, we examined two samples: PBM and PrCe5. The PrCe5 sample exhibits a slightly smaller impedance, approximately 1.2 Ω cm², compared to the PBM sample, which shows around 1.4 Ω cm². This indicates that there is no noticeable impact of Ce-doping on these samples. Indeed, Ce doping at the *A* site of perovskites may not significantly enhance electrocatalytic properties due to limited redox activity, minimal impact on the electronic structure, and doping concentration limits. The *B* site, typically hosting metals active in redox reactions, plays a more crucial role in determining the electrocatalytic performance of perovskites. The ASR values change over time, as suggested from the slight prolonged "tail" seen in the last data points, which stabilizes around 10 minutes.

Shifting to the 3.5 µm-GDC buffer layer, the three samples, PBM, PrCe5, and PrCe5Ni, revealed interesting trends. The impedance of PBM is reduced, ASR ~ 0.7 Ω cm², in comparison with the 1 µm-GDC case. PrCe5 has a similar impedance to the 1 µm-GDC situation, with an ASR ~ 0.9 Ω cm². The addition of nickel to the PrCe5 composition has markedly enhanced its

electrical characteristics, reducing the impedance by approximately half when compared to PrCe5. The area-specific resistance (ASR) of PrCe5Ni is ~ 0.5 Ω cm², notably lower than the 0.9 Ω cm² measured in PrCe5. The small semicircle at high frequencies for the PrCe5Ni electrode is derived from the charge transfer process. Its low impedance suggests that the charge transfer process is efficient, likely due to a combined effect of the improved electrode surface properties by Ce-doping (see paragraph 4.2) and catalytic effect provided by nickel dopant. The larger low frequency semicircle might be associated with surface adsorption/dissociation of H_2 process. Clearly, the presence of Ni (e.g., 3.5 µm-GDC case), which is known to be a good catalyst to H-spillover, helps reduce the impedance of this low-frequency process.
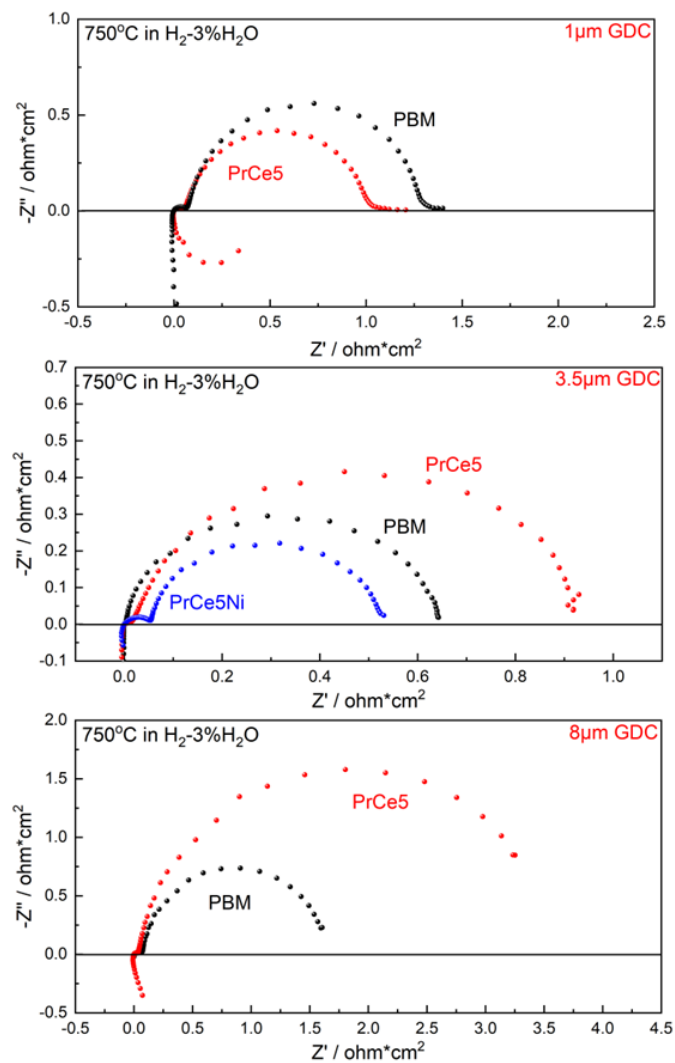

Figure 5. Nyquist plots for electrodes on GDC buffer layer with different thicknesses.

When examining the 8 µm-GDC buffer layers, where the PBM and PrCe5 samples were studied, a different behavior is observed. The PrCe5 sample shows a significantly broadened arc than in the 1 µm and 3 µm scenarios. The ASR for PBM is ~ 1.6 Ω cm², while PrCe5 has a remarkably higher value, ASR ~ 3.5 Ω cm². This indicates a substantial variation in electrochemical performance with increased GDC buffer layer thickness, underscoring the complex interplay between material composition and structural dimensions in these systems. The variations in electrochemical performance observed with the 8 µm-GDC buffer layers, particularly the high ASR values for the PrCe5 sample, prompt further investigation into the structural integrity of the cell components. The SEM analysis shown in Figure S13 reveals that the 8 µm-GDC buffer layers, initially well-bonded and uniformly covering the YSZ substrate, experienced peeling, and flaking. This delamination, likely attributable to the thermal expansion coefficient mismatch between GDC and YSZ,[5, 55] evidently impacts the stability of the cell and contributes to the observed decrease in electrochemical performance in the thicker GDC buffer layer samples.

4.2 Microstructure analysis for the PBM and PrCe5 electrodes on 3.5 µm-GDC

Figure 6 shows microstructure images of PBM and PrCe5 anodes sintered 3.5 µm-GDC before and after hydrogen testing for 200 h. After testing the PBM electrode exhibits a rougher surface with significant grain growth, increased agglomeration, and reduced porosity, suggesting extensive sintering or material consolidation. In contrast, while the PrCe5 anode also shows grain enlargement and smoothing of particle edges, it maintains more distinct grain boundaries, and appears to experience less agglomeration and reduction in porosity. These morphological alterations indicate that PrCe5 exhibits a more favorable response than PBM to hydrogen environments, particularly in terms of microstructural evolution and coarsening. This disparity, attributable to cerium doping, may substantially influence the performance of the anodes.
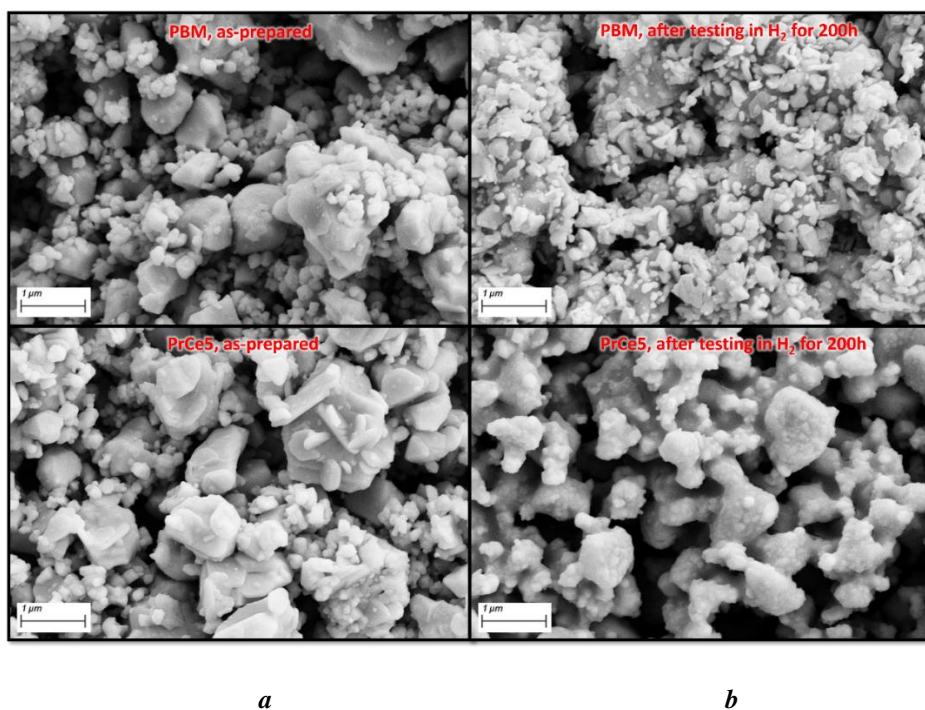
a   *b*

Figure 6. SEM of the PBM and PrCe5 electrodes surfaces (a) before and (b) after 200 h-hydrogen tests.

Figures 7a & b and S14 showcase SEM images alongside EDS barium mapping of the PBM electrode's cross-section, taken before and after hydrogen exposure. These images reveal a modest diffusion of barium cations through the GDC buffer layer. It is well-established that in electrode materials rich in barium, such as in $Ba_{0.5}Sr_{0.5}Co_{0.8}Fe_{0.2}O_{3-\delta}$, the diffusion of Ba^{2+} ions typically takes place within a temperature spectrum of 850 to 900 ° C.[47, 56] This ion diffusion, while observed to a minor extent in the PBM electrode, did not immediately impact its performance during a 200-hour hydrogen test. However, the potential for affecting long-term stability is a concern due to this diffusion.

On the other hand, no signs of cation diffusion were observed in the PrCe5 electrode, as demonstrated in Figures 7c and d. This lack of diffusion implies enhanced long-term stability of the electrode under test conditions. The introduction of cerium into $PrBaMn_2O_5$ enhances its microstructural stability, a phenomenon attributed to the interplay between defect chemistry and changes in the crystal structure. This is further supported by Malavasi's research on perovskite manganites, which highlights the significant role of defect chemistry in such

materials.[57] The ability of cerium to alternate between the Ce^{3+} and Ce^{4+} oxidation states leads to the creation of point defects, such as oxygen vacancies. These defects serve as "pinning" centers that restrict grain growth, thus improving the microstructural stability at high temperatures. Regarding the crystal structure, the incorporation of cerium introduces a nuanced disparity in ionic radii compared to Pr^{3+} (Ce^{3+} at 1.14 Å and Ce^{4+} at 0.97 Å vs. Pr^{3+} at 1.13 Å),[35] fostering local lattice distortions. These distortions impede the diffusion of atoms and defects, thereby inhibiting grain growth and microstructural alterations and elevate the activation energy required for such processes, enhancing material stability. Cerium doping also changes the chemical and local electronic structures within $PrBaMn_2O_5$, potentially enhancing the stability of its grain boundaries. The contrast between the stability of the PrCe5 and PBM electrodes underscores the critical role of selective elemental doping, defect chemistry and crystal structure modifications in optimizing the performance and longevity of electrode materials.
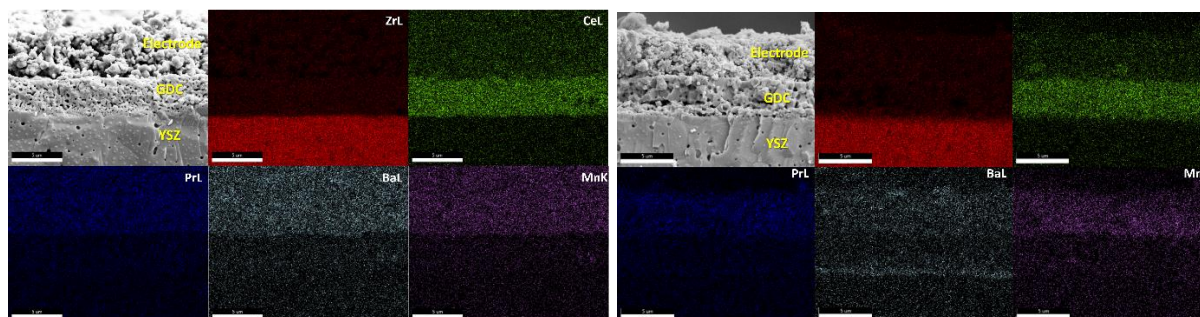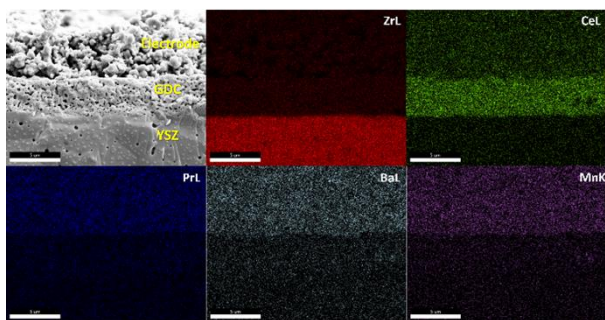

PBM electrode: *a*   *b*
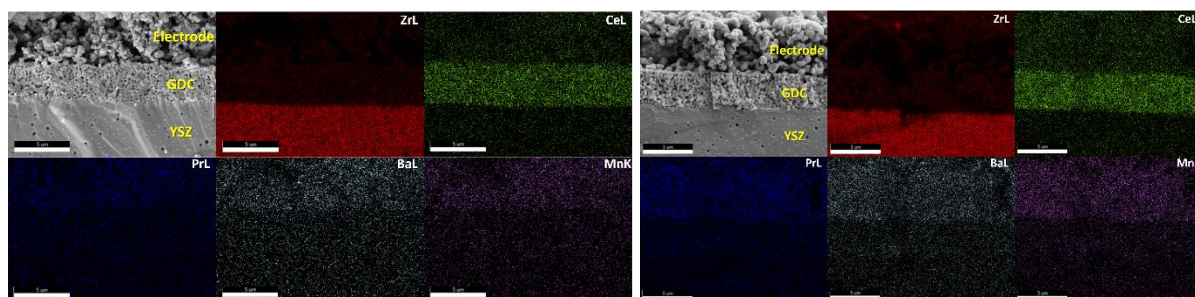
 PrCe5 electrode: *c*   *d*

Figure 7. Cross-section SEM images and EDS element mapping of PBM and PrCe5 electrodes deposited on 3.5 µm-GDC: Panels (a) and (c) depict the pre-test baseline, whereas panels (b) and (d) show the state following 200 h of H_2 exposure.

4.3 Time evolution of the impedance spectra

Nyquist plots for the PrCe5 1 µm-GDC cell, illustrated in Figure S15, demonstrate a progressive increase in polarization resistance over time, suggesting potential electrochemical stability issues. Comparison of X-ray diffraction patterns of the electrode surface, before and after hydrogen exposure (Figure S16), reveals chemical degradation and the formation of new phases. This degradation cannot be attributed to the electrode material's exposure to high temperatures in a hydrogen environment. Interestingly, electrodes integrated on an 8 µm-thick GDC buffer layer also show instability issues (Figure S17), yet without any signs of chemical degradation after identical prolonged hydrogen exposure, as evidenced in Figure S18. The degradation seen with the 1 µm buffer layer mainly stems from the migration of Ba^{2+} ions from the electrode towards the YSZ electrolyte, a phenomenon observed to a much lesser extent in PBM electrodes with a 3.5 µm-GDC buffer (Figure 7b). This migration significantly compromises the electrode/electrolyte interface's integrity.

For cells with an 8 µm-GDC buffer, SEM images of the electrode cross-section before and after electrochemical testing in hydrogen, presented in Figure S19, reveal clear signs of partial delamination between the electrode and the GDC layer. This delamination contributes to the observed increase in ASR over time (Figure S17).

Figure 8 summarizes the ASR evolution over time for PBM, PrCe5, and PrCeNi electrodes under H_2 at 750 °C, across GDC buffer layers of 1 µm, 3.5 µm, and 8 µm. With 1 µm-GDC, PBM and PrCe5 experience a rapid R_p increase, estimated at 0.15-0.2 Ω cm^2 h^{-1}. At 3.5 µm, all electrodes maintain stable R_p values, with an estimated increase of $\sim$ 0.002 Ω cm^2 h^{-1}. With 8

µm, PBM shows moderate ASR increases, while PrCe5 remains stable. Those results suggest a 3.5 µm-GDC layer as optimal for praseodymium barium double perovskite manganite electrodes in SOFC anodes, differing from previous studies of Briois *et al*. recommending ~ 0.57 µm- GDC layer.[32] The 3.5 µm-GDC layer thickness achieves the lowest ASR after 220 hours at $T = 750$ °C for our Ba-rich double layered perovskite anodes in a hydrogen environment, supporting the effectiveness of 2-4 µm GDC layers for SOFC anode performance and mass production, reported previouly.[58]
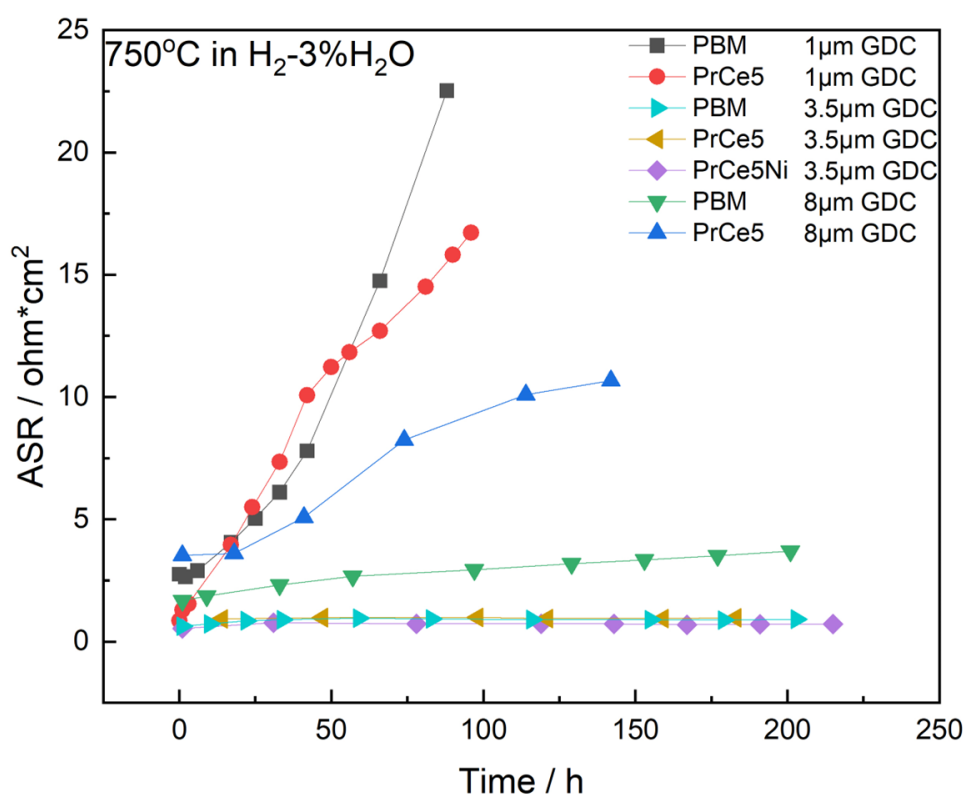

Figure 8. **Impact of GDC buffer layer thickness on ASR performance over time for PBM, PrCe5 and PrCe5Ni anodes.**

5. Conclusion

Our investigation into the effects of cerium doping on the $PrBaMn_2O_{5+\delta}$ (PBM) structure, both in the absence and presence of nickel, for SOFC anodes has shown promising enhancements in performance and stability. The introduction of cerium, particularly at a concentration of 5 at. %, markedly improves the electrochemical efficiency and microstructural integrity of the

anode. This improvement is evidenced by a decrease in ASR, better thermal expansion coefficient, prevention of Ba^{2+} cation diffusion-especially across the optimally 3.5 µm thick GDC buffer layer- and reduced agglomeration and porosity after 200 h exposure to hydrogen. Additionally, the inclusion of nickel results in a 50% reduction in ASR. The combined effect of cerium and nickel co-doping, which is deeply rooted in the essential roles of defect chemistry and crystal structure, underscores the importance of these domains in the development of advanced materials for energy applications.

Supporting Information

- Variations in lattice parameters with cerium content and detailed lattice parameters of as-prepared and oxidized layered perovskites.
- Rietveld refinements of PrCe5Ni before and after hydrogen reduction and after reoxidation
- XRD for thermal treatments of PrCe5/GDC and PrCe5/YSZ composites
- Temperature-dependent Neutron Powder Diffraction and TEC for PrCe5/YSZ
- Scanning Electron Microscopy and Energy Dispersive Spectroscopy mapping after hydrogen testing.
- XRD before and after 100 hours of hydrogen testing.
- Electrochemical performance using Nyquist plots.

Acknowledgements

References

1.   Ruiz-Morales, J. C.; Canales-Vázquez, J.; Ballesteros-Pérez, B.; Peña-Martínez, J.; Marrero-López, D.; Irvine, J. T. S.; Núñez, P., LSCM–(YSZ–CGO) composites as improved symmetrical electrodes for solid oxide fuel cells. *Journal of the European Ceramic Society* **2007,** 27, (13), 4223-4227.

2.   Deleebeeck, L.; Fournier, J. L.; Birss, V., Comparison of Sr-doped and Sr-free La1−xSrxMn0.5Cr0.5O3±δ SOFC Anodes. *Solid State Ionics* **2010,** 181, (25), 1229-1237.

3.   Ormerod, R. M., Solid oxide fuel cells. *Chemical Society Reviews* **2003,** 32, (1), 17-28.

4.   Minh, N. Q., Solid oxide fuel cell technology—features and applications. *Solid State Ionics* **2004,** 174, (1), 271-277.

5.   Huang, K.; Goodenough, J. B., 9 - Performance characterization techniques for a solid oxide fuel cell (SOFC) and its components. In *Solid Oxide Fuel Cell Technology*, Huang, K.; Goodenough, J. B., Eds. Woodhead Publishing: 2009; pp 156-182.

6.   Huang, K.; Goodenough, J. B., *Solid Oxide Fuel Cell Technology: Principles, Performance And Operations*. Woodhead Publishing: 2009; p 340.

7.   Huang, K.; Lee, H. Y.; Goodenough, J. B., Sr- and Ni-Doped LaCoO3 and LaFeO3 Perovskites: New Cathode Materials for Solid-Oxide Fuel Cells. *Journal of The Electrochemical Society* **1998,** 145, (9), 3220-3227.

8.   Hubert, M.; Laurencin, J.; Cloetens, P.; Morel, B.; Montinaro, D.; Lefebvre-Joud, F., Impact of Nickel agglomeration on Solid Oxide Cell operated in fuel cell and electrolysis modes. *Journal of Power Sources* **2018,** 397, 240-251.

9.   Fuerte, A.; Valenzuela, R. X.; Escudero, M. J.; Daza, L., Effect of cobalt incorporation in copper-ceria based anodes for hydrocarbon utilisation in Intermediate Temperature Solid Oxide Fuel Cells. *Journal of Power Sources* **2011,** 196, (9), 4324-4331.

10.   Sfeir, J.; Buffat, P. A.; Möckli, P.; Xanthopoulos, N.; Vasquez, R.; Joerg Mathieu, H.; Van herle, J.; Ravindranathan Thampi, K., Lanthanum Chromite Based Catalysts for Oxidation of Methane Directly on SOFC Anodes. *Journal of Catalysis* **2001,** 202, (2), 229-244.

11.   Atkinson, A.; Barnett, S.; Gorte, R. J.; Irvine, J. T. S.; McEvoy, A. J.; Mogensen, M.; Singhal, S. C.; Vohs, J., Advanced anodes for high-temperature fuel cells. In *Materials for Sustainable Energy*, Co-Published with Macmillan Publishers Ltd, UK: 2010; pp 213-223.

12.	Skinner, S. J.; Packer, R. J.; Bayliss, R. D.; Illy, B.; Prestipino, C.; Ryan, M. P., Redox chemistry of the novel fast oxide ion conductor CeNbO4+d determined through an in-situ spectroscopic technique. *Solid State Ionics* **2011,** 192, (1), 659-663.

13.	Lay, E.; Benamira, M.; Pirovano, C.; Gauthier, G.; Dessemond, L., Effect of Ce-Doping on the Electrical and Electrocatalytical Behavior of La/Sr Chromo-Manganite Perovskite as New SOFC Anode. *Fuel Cells* **2012,** 12, (2), 265-274.

14.	Lay, E.; Dessemond, L.; Gauthier, G. H., Synthesis and Characterization of CexSr1-xCr0.5Mn0.5O3-δ Perovskites as Anode Materials for Solid Oxide Fuel Cells (SOFC). *Electrochimica Acta* **2016,** 216, 420-428.

15.	Ran, R.; Wu, X. D.; Quan, C. Z.; Weng, D., Effect of strontium and cerium doping on the structural and catalytic properties of PrMnO$_3$ oxides. *SOLID STATE IONICS* **2005,** 176, (9-10), 965-971.

16.	Zhou, X.-W.; Sun, Y.-F.; Wang, G.-Y.; Gao, T.; Chuang, K. T.; Luo, J.-L.; Chen, M.; Birss, V. I., Synthesis and electrocatalytic performance of La0.3Ce0.1Sr0.5Ba0.1TiO3 anode catalyst for solid oxide fuel cells. *Electrochemistry Communications* **2014,** 43, 79-82.

17.	Périllat-Merceroz, C.; Gauthier, G.; Roussel, P.; Huvé, M.; Gélin, P.; Vannier, R.-N., Synthesis and Study of a Ce-Doped La/Sr Titanate for Solid Oxide Fuel Cell Anode Operating Directly on Methane. *Chemistry of Materials* **2011,** 23, (6), 1539-1550.

18.	Shen, J.; Yang, G.; Zhang, Z.; Zhou, W.; Wang, W.; Shao, Z., Tuning layer-structured La0.6Sr1.4MnO4+δ into a promising electrode for intermediate-temperature symmetrical solid oxide fuel cells through surface modification. *Journal of Materials Chemistry A* **2016,** 4, (27), 10641-10649.

19.	Jiang, S. P., A review of wet impregnation—An alternative method for the fabrication of high performance and nano-structured electrodes of solid oxide fuel cells. *Materials Science and Engineering: A* **2006,** 418, (1), 199-210.

20.	Bahout, M.; Managutti, P. B.; Dorcet, V.; Le Gal La Salle, A.; Paofai, S.; Hansen, T. C., In situ exsolution of Ni particles on the PrBaMn2O5 SOFC electrode material monitored by high temperature neutron powder diffraction under hydrogen. *Journal of Materials Chemistry A* **2020,** 8, (7), 3590-3597.

21.	Kwon, O.; Sengodan, S.; Kim, K.; Kim, G.; Jeong, H. Y.; Shin, J.; Ju, Y.-W.; Han, J. W.; Kim, G., Exsolution trends and co-segregation aspects of self-grown catalyst nanoparticles in perovskites. *Nature Communications* **2017,** 8, 15967.

22.	Gu, Y.; Zhang, Y.; Zheng, Y.; Chen, H.; Ge, L.; Guo, L., PrBaMn2O5+δ with praseodymium oxide nano-catalyst as electrode for symmetrical solid oxide fuel cells. *Applied Catalysis B: Environmental* **2019,** 257, 117868.

23.	Tsoga, A.; Naoumidis, A.; Stöver, D., Total electrical conductivity and defect structure of ZrO2–CeO2–Y2O3–Gd2O3 solid solutions. *Solid State Ionics* **2000,** 135, (1), 403-409.

24.	Xu, G.; Ma, H.; Zhong, M.; Zhou, J.; Yue, Y.; He, Z., Influence of pH on characteristics of BaFe12O19 powder prepared by sol–gel auto-combustion. *Journal of Magnetism and Magnetic Materials* **2006,** 301, (2), 383-388.

25.	Roisnel, T.; Rodriguez-Carvajal, J., WinPLOTR: A Windows tool for powder diffraction pattern analysis. In *Epdic 7: European Powder Diffraction, Pts 1 and 2*, Delhez, R.; Mittemeijer, E. J., Eds. 2001; Vol. 378-3, pp 118-123.

26.	Hansen, T. C.; Henry, P. F.; Fischer, H. E.; Torregrossa, J.; Convert, P., The D20 instrument at the ILL: a versatile high-intensity two-axis neutron diffractometer. *Measurement Science and Technology* **2008,** 19, (3), 034001.

27.	Tonus, F.; Bahout, M.; Battle, P. D.; Hansen, T.; Henry, P. F.; Roisnel, T., In situ neutron diffraction study of the high-temperature redox chemistry of Ln(3-x)Sr(1+x)CrNiO(8-delta) (Ln = La, Nd) under hydrogen. *Journal of Materials Chemistry* **2010,** 20, (20), 4103-4115.

28.	Managutti, P. B.; Yu, H.; Hernandez, O.; Prestipino, C.; Dorcet, V.; Wang, H.; Hansen, T. C.; Bahout, M., Exsolution of Co–Fe Alloy Nanoparticles on the PrBaFeCoO5+δ Layered Perovskite Monitored by Neutron Powder Diffraction and Catalytic Effect on Dry Reforming of Methane. *ACS Applied Materials & Interfaces* **2023,** 15, (19), 23040-23050.

29.   Managutti, P. B.; Tymen, S.; Liu, X.; Hernandez, O.; Prestipino, C.; Le Gal La Salle, A.; Paul, S.; Jalowiecki-Duhamel, L.; Dorcet, V.; Billard, A.; Briois, P.; Bahout, M., Exsolution of Ni Nanoparticles from A-Site-Deficient Layered Double Perovskites for Dry Reforming of Methane and as an Anode Material for a Solid Oxide Fuel Cell. *ACS Applied Materials & Interfaces* **2021,** 13, (30), 35719-35728.

30.   Rodríguez-Carvajal, J., Recent advances in magnetic structure determination by neutron powder diffraction. *Physica B: Condensed Matter* **1993,** 192, (1-2), 55-69.

31.   Bérar, J. F.; Lelann, P., E.s.d.'s and estimated probable error obtained in Rietveld refinements with local correlations. *Journal of Applied Crystallography* **1991,** 24, (1), 1-5.

32.   Bouleau, L.; Coton, N.; Coquoz, P.; Ihringer, R.; Billard, A.; Briois, P., GDC Buffer Layer Synthesized by Reactive Magnetron Sputtering: Effect of Total Pressure and Thickness on SOFC Performances. *Crystals* **2020,** 10, (9), 759.

33.   Breaz, E.; Aubry, E.; Billard, A.; Coton, N.; Coquoz, P.; Pappas, A.; Diethelm, S.; Ihringer, R.; Briois, P., Influence of the Bias Substrate Power on the GDC Buffer Layer. *ECS Transactions* **2017,** 78, (1), 807-815.

34.   Tsoga, A.; Gupta, A.; Naoumidis, A.; Nikolopoulos, P., Gadolinia-doped ceria and yttria stabilized zirconia interfaces: regarding their application for SOFC technology. *Acta Materialia* **2000,** 48, (18), 4709-4714.

35.   Shannon, R. D., Revised effective ionic radii and systematic studies of interatomic distances in halides and chalcogenides. *Acta Crystallographica Section A* **1976,** 32, (5), 751-767.

36.   Cox-Galhotra, R. A.; Huq, A.; Hodges, J. P.; Yu, C.; Wang, X.; Gong, W.; Jacobson, A. J.; McIntosh, S., An in-situ neutron diffraction study of the crystal structure of $PrBaCo_2O_{5+\delta}$ at high temperature and controlled oxygen partial pressure. *Solid State Ionics* **2013,** 249–250, 34-40.

37.   Tomkiewicz, A. C.; Tamimi, M. A.; Huq, A.; McIntosh, S., Structural analysis of $PrBaMn_2O_{5+\delta}$ under SOFC anode conditions by in-situ neutron powder diffraction. *Journal of Power Sources* **2016,** 330, 240-245.

38.   Pineda, O. L.; Moreno, Z. L.; Roussel, P.; Świerczek, K.; Gauthier, G. H., Synthesis and preliminary study of the double perovskite $NdBaMn_2O_{5+\delta}$ as symmetric SOFC electrode material. *Solid State Ionics* **2016,** 288, 61-67.

39.   Shin, T. H.; Myung, J.-H.; Verbraeken, M.; Kim, G.; Irvine, J. T. S., Oxygen deficient layered double perovskite as an active cathode for CO_2 electrolysis using a solid oxide conductor. *Faraday Discussions* **2015,** 182, (0), 227-239.

40.   Bahout, M.; Pramana, S. S.; Hanlon, J. M.; Dorcet, V.; Smith, R. I.; Paofai, S.; Skinner, S. J., Stability of $NdBaCo_{2-x}Mn_xO_{5+}$[small delta] (x = 0, 0.5) layered perovskites under humid conditions investigated by high-temperature in situ neutron powder diffraction. *Journal of Materials Chemistry A* **2015,** 3, (30), 15420-15431.

41.   Jeamjumnunja, K.; Gong, W.; Makarenko, T.; Jacobson, A. J., A determination of the oxygen non-stoichiometry of the oxygen storage materials $LnBaMn_2O_{5+\delta}$ (Ln=Gd, Pr). *Journal of Solid State Chemistry* **2016,** 239, 36-45.

42.   Trukhanov, S. V.; Lobanovski, L. S.; Bushinsky, M. V.; Fedotova, V. V.; Troyanchuk, I. O.; Trukhanov, A. V.; Ryzhov, V. A.; Szymczak, H.; Szymczak, R.; Baran, M., Study of A-site ordered $PrBaMn_2O_{6-\delta}$ manganite properties depending on the treatment conditions. *Journal of Physics: Condensed Matter* **2005,** 17, (41), 6495.

43.   Sengodan, S.; Choi, S.; Jun, A.; Shin, T. H.; Ju, Y.-W.; Jeong, H. Y.; Shin, J.; Irvine, J. T. S.; Kim, G., Layered oxygen-deficient double perovskite as an efficient and stable anode for direct hydrocarbon solid oxide fuel cells. *Nat Mater* **2015,** 14, (2), 205-209.

44.   Faes, A.; Hessler-Wyser, A.; Zryd, A.; Van herle, J., A Review of RedOx Cycling of Solid Oxide Fuel Cells Anode. *Membranes* **2012,** 2, (3), 585.

45.   Sun, Y.-F.; Zhou, X.-W.; Zeng, Y.; Amirkhiz, B. S.; Wang, M.-N.; Zhang, L.-Z.; Hua, B.; Li, J.; Li, J.-H.; Luo, J.-L., An ingenious Ni/Ce co-doped titanate based perovskite as a coking-tolerant anode material for direct hydrocarbon solid oxide fuel cells. *Journal of Materials Chemistry A* **2015,** 3, (45), 22830-22838.

46.   Castillo-Martínez, E.; Williams, A. J.; Attfield, J. P., High-temperature neutron diffraction study of the cation ordered perovskites TbBaMn2O5+x and TbBaMn2O5.5−y. *Journal of Solid State Chemistry* **2006,** 179, (11), 3505-3510.

47.   Duan, Z.; Yang, M.; Yan, A.; Hou, Z.; Dong, Y.; Chong, Y.; Cheng, M.; Yang, W., Ba0.5Sr0.5Co0.8Fe0.2O3−δ as a cathode for IT-SOFCs with a GDC interlayer. *Journal of Power Sources* **2006,** 160, (1), 57-64.

48.   Kim, Y.-M.; Kim-Lohsoontorn, P.; Bae, J., Effect of unsintered gadolinium-doped ceria buffer layer on performance of metal-supported solid oxide fuel cells using unsintered barium strontium cobalt ferrite cathode. *Journal of Power Sources* **2010,** 195, (19), 6420-6427.

49.   Hayashi, H.; Saitou, T.; Maruyama, N.; Inaba, H.; Kawamura, K.; Mori, M., Thermal expansion coefficient of yttria stabilized zirconia for various yttria contents. *Solid State Ionics* **2005,** 176, (5–6), 613-619.

50.   Tietz, F., Thermal expansion of SOFC materials. *Ionics* **1999,** 5, (1), 129-139.

51.   Zhang, S.-L.; Wang, H.; Lu, M. Y.; Zhang, A.-P.; Mogni, L. V.; Liu, Q.; Li, C.-X.; Li, C.-J.; Barnett, S. A., Cobalt-substituted SrTi0.3Fe0.7O3−δ: a stable high-performance oxygen electrode material for intermediate-temperature solid oxide electrochemical cells. *Energy & Environmental Science* **2018,** 11, (7), 1870-1879.

52.   Naiqing, Z.; Kening, S.; Derui, Z.; Dechang, J., Study on Properties of LSGM Electrolyte Made by Tape Casting Method and Applications in SOFC. *Journal of Rare Earths* **2006,** 24, (1, Supplement 1), 90-92.

53.   Tompsett, G. A.; Sammes, N. M.; Yamamoto, O., Ceria–Yttria-Stabilized Zirconia Composite Ceramic Systems for Applications as Low-Temperature Electrolytes. *Journal of the American Ceramic Society* **1997,** 80, (12), 3181-3186.

54.   Hayashi, H.; Kanoh, M.; Quan, C. J.; Inaba, H.; Wang, S.; Dokiya, M.; Tagawa, H., Thermal expansion of Gd-doped ceria and reduced ceria. *Solid State Ionics* **2000,** 132, (3–4), 227-233.

55.   Hussain, S.; Yangping, L., Review of solid oxide fuel cell materials: cathode, anode, and electrolyte. *Energy Transitions* **2020,** 4, (2), 113-126.

56.   Qingshan, Z.; Tongan, J.; Yong, W., Thermal expansion behavior and chemical compatibility of BaxSr1−xCo1−yFeyO3−δ with 8YSZ and 20GDC. *Solid State Ionics* **2006,** 177, (13), 1199-1204.

57.   Malavasi, L., Role of defect chemistry in the properties of perovskite manganites. *Journal of Materials Chemistry* **2008,** 18, (28), 3295-3308.

58.   Hussain, A.; Song, R.-H.; Khan, M. Z.; Kim, T.-H.; Hong, J.-E.; Joh, D. W.; Ishfaq, H. A.; Lee, S.-B.; Lim, T.-H., Durability improvement of large-area anode supported solid oxide fuel cell fabricated by 4-layer sequential co-lamination and co-firing process. *Journal of Power Sources* **2023,** 573, 233160.